Angle-domain illumination gathers by wave-equation-based methods

Yaxun Tang and Biondo Biondi

ABSTRACT

We present a method for computing the wave-equation-based angle-domain illumination for subsurface structures. It creates subsurface illumination for different scattering or/and dip angles for a given acquisition geometry, velocity model and frequency bandwidth. The proposed method differs from the conventional method in that it does not require local plane-wave decompositions for each source and receiver Green's functions. Instead, it transforms a precomputed subsurface-offset-indexed sensitivity kernel into angle domain using either a Fourier-domain mapping or a space-domain slant stack. We show that the computational cost can be significantly reduced by phase encoding the receiver-side Green's functions, or by simultaneously encoding both the source- and receiver-side Green's functions. Numerical examples demonstrate the accuracy and efficiency of our method. The main anticipated applications of our method are in areas of: (1) accurate amplitude-versus-angle (AVA) analysis by compensating depth-migrated images with angle-dependent illumination, (2) migration velocity analysis that incorporates angle-dependent illumination for robust residual parameter estimation, and (3) optimum seismic survey planning.

INTRODUCTION

Seismic image quality obtained using prestack depth migration is highly dependent on subsurface illumination, which can be affected by many factors, e.g., the limited acquisition geometry, the complex velocity model, and the frequency content of seismic waves. Uneven illumination causes distorted seismic images due to the fact that migration operator is nonunitary (Nemeth et al., 1999; Clapp, 2005; Valenciano, 2008; Tang, 2009). Seismic illumination analysis quantifies such image distortion and provides ways to optimally restore the reflectivity. More accurate amplitude-versus-angle (AVA) analysis can be obtained if the angle-domain common-image gather is corrected with angle-dependent illumination. Angle-domain velocity analysis may also benefit from angle-dependent illumination weighting. It can weight up well-illuminated angular images, while weight down poorly-illuminated ones for robust residual parameter estimation, reducing the uncertainty caused by poor illumination.

Angle-domain illumination analysis is often carried out using ray-based method due to its efficiency (Schneider and Winbow, 1999; Bear et al., 2000). However,

the infinite-frequency approximation and the caustics inherent in ray theory prevent ray-based method from accurately modeling complex wave phenomena. Wave-equation-based method, on the other hand, more accurately describes bandlimited wave phenomena, and therefore more suitable for complex geologies, e.g., subsalt regions with complex overburdens. Wave-equation-based angle-domain illumination analysis is proposed by Xie et al. (2006), where local plane-wave decomposition has been employed to extract the directional information for both source and receiver Green's functions before spatial and temporal correlations.

In this paper, we present an alternative way of computing the angle-dependent illumination. Instead of performing local plane-wave decomposition for each Green's function, our method transforms a subsurface-offset-indexed sensitivity kernel into the angle domain and then correlating the corresponding angle-domain sensitivity kernel to produce the angle-dependent illumination. The procedure closely resembles the method of Sava and Fomel (2003), which computes angle-dependent reflectivity image after imaging using a Fourier-domain mapping. We demonstrate in two dimensions that our method generates the scattering-angle illumination suitable for point scatterers if only horizontal subsurface offset has been computed. For planar reflectors, however, dip-dependent scattering-angle illumination is necessary, instead of scattering-angle illumination that averages over all dips. We show that the dip-dependent scattering-angle-domain illumination gather can be obtained by mapping either midpoint wavenumbers or subsurface-offset wavenumbers that contain both horizontal and vertical subsurface offsets.

In fact, the subsurface illumination that we often refer to is only a subset, or more precisely, the diagonal part of the imaging Hessian matrix. The off-diagonal components of the Hessian have been proven useful when applied to improve images of extremely poor illumination, e.g., subsalt regions with shadow zones (Valenciano, 2008; Tang, 2009). Our method discussed here also allows us to compute the off-diagonal components of the angle-domain imaging Hessian in a target-oriented fashion, hence it can be used to invert for the angle-domain reflectivity in a model-domain least-squares migration/inversion. A naive implementation of the proposed method, however, can be prohibitively expensive with the computational cost proportional to the number of sources, receivers and frequencies. We show how the phase-encoding technique (Tang, 2008b,a, 2009) is able to make the method more cost effective.

This paper is organized as follows: we first review the theory of computing the illumination, or more generally, the imaging Hessian, in the subsurface-offset domain. Then we demonstrate how to transform the sensitivity kernel into angle-domain and how to compute the scattering-angle-domain Hessian, as well as the dip-dependent scattering-angle-domain Hessian. Finally we apply our method to the Sigsbee2A model.

SUBSURFACE-OFFSET-DOMAIN IMAGE AND ILLUMINATION

Linearized modeling (Born modeling) from a prestack image parameterized as a function of subsurface offset can be described as follows:

$$d(\mathbf{x}_r, \mathbf{x}_s, \omega) = \sum_{\mathbf{x}} \sum_{\mathbf{h}} L_h(\mathbf{x}, \mathbf{h}, \mathbf{x}_r, \mathbf{x}_s, \omega) m_h(\mathbf{x}, \mathbf{h}), \tag{1}$$

where $d(\mathbf{x}_r, \mathbf{x}_s, \omega)$ is the seismic data with a source located at $\mathbf{x}_s = (x_s, y_s, z_s = 0)$ and a receiver located at $\mathbf{x}_r = (x_r, y_r, z_r = 0)$; ω is the angular frequency; $m_h(\mathbf{x}, \mathbf{h})$ is the prestack image located at $\mathbf{x} = (x, y, z)$ for a half subsurface offset $\mathbf{h} = (h_x, h_y, h_z)$; L_h is the sensitivity kernel defined as follows:

$$L_h(\mathbf{x}, \mathbf{h}, \mathbf{x}_r, \mathbf{x}_s, \omega) = \omega^2 f_s(\omega) G(\mathbf{x} - \mathbf{h}, \mathbf{x}_s, \omega) G(\mathbf{x} + \mathbf{h}, \mathbf{x}_r, \omega), \tag{2}$$

where $f_s(\omega)$ is the source signature, and $G(\mathbf{x}, \mathbf{x}_s, \omega)$ and $G(\mathbf{x}, \mathbf{x}_r, \omega)$ are the Green's functions connecting the source and receiver, respectively, to the image point $\mathbf{x}$.

Reconstruction of the prestack image $m(\mathbf{x}, \mathbf{h})$ can be posed as an inverse problem by minimizing the following objective function defined in the data space:

$$F(\mathbf{m}) = \frac{1}{2} \sum_{\omega} \sum_{\mathbf{x}_s} \sum_{\mathbf{x}_r} |W(\mathbf{x}_r, \mathbf{x}_s) r(\mathbf{x}_r, \mathbf{x}_s, \omega)|^2, \tag{3}$$

where $r(\mathbf{x}_r, \mathbf{x}_s, \omega) = d(\mathbf{x}_r, \mathbf{x}_s, \omega) - d_{\text{obs}}(\mathbf{x}_r, \mathbf{x}_s, \omega)$ is the data residual and $W(\mathbf{x}_r, \mathbf{x}_s)$ is the acquisition mask operator, which contains unity values where we record data and zeros where we do not. The gradient of the objective function F reads

$$I_h(\mathbf{x}, \mathbf{h}) = \sum_{\omega} \sum_{\mathbf{x}_s} \sum_{\mathbf{x}_r} W^2(\mathbf{x}_r, \mathbf{x}_s) L_h^*(\mathbf{x}, \mathbf{h}, \mathbf{x}_r, \mathbf{x}_s, \omega) r(\mathbf{x}_r, \mathbf{x}_s, \omega), \tag{4}$$

where * denotes complex conjugation. Equation 4 is similar to the prestack shot-profile migration formula and it produces migrated reflectivity images defined in the subsurface offset domain (Rickett and Sava, 2002).

The Hessian can be obtained by taking the second-order derivatives of F with respect to the model parameters as follows:

$$H_h(\mathbf{x}, \mathbf{x}', \mathbf{h}, \mathbf{h}') = \sum_{\omega} \sum_{\mathbf{x}_s} \sum_{\mathbf{x}_r} W^2(\mathbf{x}_r, \mathbf{x}_s) L_h^*(\mathbf{x}, \mathbf{h}, \mathbf{x}_r, \mathbf{x}_s, \omega) L_h(\mathbf{x}', \mathbf{h}', \mathbf{x}_r, \mathbf{x}_s, \omega). \tag{5}$$

When $\mathbf{x} = \mathbf{x}'$ and $\mathbf{h} = \mathbf{h}'$, we obtain the diagonal elements of the Hessian operator

$$H_h(\mathbf{x}, \mathbf{h}) = \sum_{\omega} \sum_{\mathbf{x}_s} \sum_{\mathbf{x}_r} W^2(\mathbf{x}_r, \mathbf{x}_s) |L_h(\mathbf{x}, \mathbf{h}, \mathbf{x}_r, \mathbf{x}_s, \omega)|^2. \tag{6}$$

The diagonal of the Hessian is often known as the illumination map of the subsurface, it contains illumination contribution from both sources and receivers for a given acquisition configuration.

ANGLE-DOMAIN IMAGE AND ILLUMINATION

Because the subsurface offset is linked to the scattering angle and dip angle through local ray parameters, the sensitivity kernel (and consequently the reflectivity image and the Hessian) can be transformed from the subsurface-offset domain into the angle domain through a simple Fourier domain mapping, or equivalently a space-domain slant stack (Sava and Fomel, 2003). In this section, we first demonstrate that a Fourier-domain mapping using the depth and horizontal-subsurface-offset wavenumbers produces scattering angles that are implicitly averaged over illuminated dips. It is useful for point scatterers. Dip-dependent scattering-angle illumination, however, is required for accurately predicting illumination strength for planar reflectors. We restrict our discussion only in 2-D for simplicity, where $\mathbf{x} = (x, z)$, $\mathbf{h} = (h_x, h_z)$, $\mathbf{x}_s = (x_s, z_s = 0)$ and $\mathbf{x}_r = (x_r, z_r = 0)$. But the extension to 3-D should be straight forward and would be discussed in further publications.

Scattering-angle-domain illumination

In a locally constant velocity medium (Figure 1), the midpoint ray parameter $\mathbf{p}_m$ and the subsurface offset ray parameter $\mathbf{p}_h$ can be expressed as follows:

$$\mathbf{p}_m = \mathbf{p}_s + \mathbf{p}_r \tag{7}$$

$$\mathbf{p}_h = \mathbf{p}_r - \mathbf{p}_s, \tag{8}$$

where $\mathbf{p}_s$ and $\mathbf{p}_r$ are the source and receiver ray parameters, respectively. Using trigonometric relations, we can further express the horizontal and vertical components of $\mathbf{p}_m$ and $\mathbf{p}_h$ as functions of the scattering angle γ that bisects the incident and the scattered rays (plane waves) and the corresponding dip angle α as follows:

$$\mathbf{p}_m = \begin{pmatrix} p_{m_x} \\ p_{m_z} \end{pmatrix} = \begin{pmatrix} 2s\cos\gamma\sin\alpha \\ -2s\cos\gamma\cos\alpha \end{pmatrix}, \tag{9}$$

and

$$\mathbf{p}_h = \begin{pmatrix} p_{h_x} \\ p_{h_z} \end{pmatrix} = \begin{pmatrix} 2s\sin\gamma\cos\alpha \\ 2s\sin\gamma\sin\alpha \end{pmatrix}, \tag{10}$$

where s is the slowness at the reflection point. Dividing p_{h_x} by p_{m_z} yields

$$\tan\gamma = -\frac{p_{h_x}}{p_{m_z}} = -\frac{k_{h_x}}{k_{m_z}}, \tag{11}$$

where k_{h_x} and k_{m_z} are vertical-subsurface-offset wavenumber and depth wavenumber, respectively. Equation 11 converts the sensitivity kernel from the subsurface-offset-domain into the scattering-angle domain. The action of the angle-domain sensitivity kernel to the data residual $r(\mathbf{x}_r, \mathbf{x}_s, \omega)$ gives the angle-domain reflectivity image. Since the Fourier-domain mapping is a linear operator and is independent from

the data residual, the sources, receivers and frequencies, it can be postponed after the subsurface-offset-domain reflectivity image is obtained. Therefore, to obtain the angle-domain reflectivity image more efficiently, we perform the mapping on the image I_h after stacking over sources, receivers and frequencies, instead of the sensitivity kernel L_h for each source, receiver and frequency (Sava and Fomel, 2003).

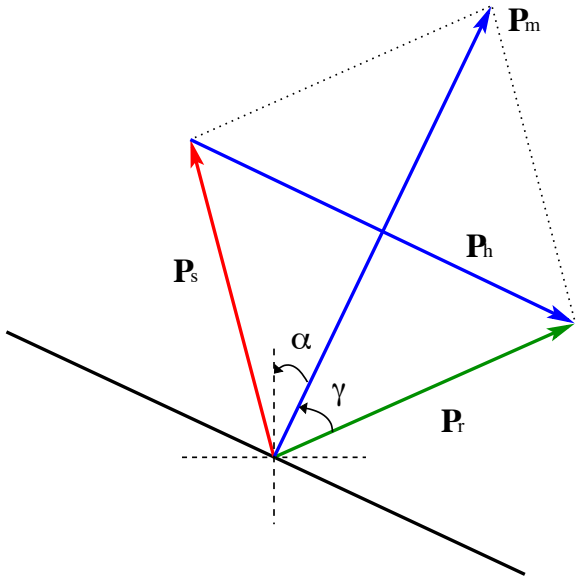

Figure 1: Geometric relations between ray vectors at a reflection point in a locally constant velocity medium. [**NR**]

We obtain the scattering-angle-domain Hessian by correlating the sensitivity kernels L_γ as follows:

$$H_\gamma(\mathbf{x},\mathbf{x}',\gamma,\gamma') = \sum_{\omega}\sum_{\mathbf{x}_s}\sum_{\mathbf{x}_r} W^2(\mathbf{x}_r,\mathbf{x}_s) L^*_\gamma(\mathbf{x},\gamma,\mathbf{x}_r,\mathbf{x}_s,\omega) L_\gamma(\mathbf{x}',\gamma',\mathbf{x}_r,\mathbf{x}_s,\omega). \quad (12)$$

The diagonal of equation 12, or the scattering-angle-domain illumination is obtained when $\mathbf{x}=\mathbf{x}'$ and $\gamma=\gamma'$

$$H_\gamma(\mathbf{x},\gamma) = \sum_{\omega}\sum_{\mathbf{x}_s}\sum_{\mathbf{x}_r} W^2(\mathbf{x}_r,\mathbf{x}_s) |L_\gamma(\mathbf{x},\gamma,\mathbf{x}_r,\mathbf{x}_s,\omega)|^2. \quad (13)$$

Contrary to the case of computing angle-domain reflectivity image, postponing the Fourier-domain mapping after stack becomes less obvious for the angle-domain Hessian computation due to the correlation term inside the summation loop in equations 12 and 13. In the following numerical examples, we take a more straight forward way that directly transforms the sensitivity kernel from the subsurface-offset domain to the scattering-angle-domain to compute the angle-domain Hessian or illumination. The steps can be summarized as follows:

- for fixed x, $\mathbf{x}_s$, $\mathbf{x}_r$ and ω, apply 2-D Fourier transform along axes z and h_x

$$L_h(x,z,h_x,\mathbf{x}_r,\mathbf{x}_s,\omega) \rightarrow L_h(x,k_z,k_{h_x},\mathbf{x}_r,\mathbf{x}_s,\omega);$$

- perform the mapping

$$L_h(x, k_z, k_{h_x}, \mathbf{x}_r, \mathbf{x}_s, \omega) \rightarrow L_\gamma(x, k_z, \gamma, \mathbf{x}_r, \mathbf{x}_s, \omega)$$

  according to relation 11;

- apply inverse 1-D Fourier transform along axis k_z

$$L_\gamma(x, k_z, \gamma, \mathbf{x}_r, \mathbf{x}_s, \omega) \rightarrow L_\gamma(x, z, \gamma, \mathbf{x}_r, \mathbf{x}_s, \omega)$$

  to obtain the scattering-angle-domain sensitivity kernel.

- compute either the scattering-angle-domain Hessian using equation 12 or the illumination using equation 13.

As a simple example, Figures 3 shows the real part of the scattering-angle-domain sensitivity kernel, converted from its subsurface-offset-domain counterpart (Figure 2). The results are obtained by using a constant velocity model (2000 m/s), and only one source (-600 m), one receiver (600 m) and one frequency (19 Hz) are computed. Figure 4 shows the corresponding single-frequency scatter-angle-domain illumination for the given velocity model and acquisition configuration. Since there are only one source and one receiver, each subsurface point is illuminated by only one scattering angle.

The scattering-angle-domain illumination is useful for point scatterers, it, however, fails to accurately predict the illumination strength for planar reflectors, where the scattered waves have preferred orientations according to the local dips of the reflectors. The reason behind this is that the transformation (equation 11) is dip-independent, the resulting angle-domain illumination implicitly averages over all dip angles and measures the overall scattering-angle illumination from all dips illuminated, instead of the illumination from one particular dip of the actual planar reflector. This point is further illustrated by Figures 5 and 6, where the computed scattering-angle-domain illumination (Figure 6(d)) accurately predicts the illumination for the point scatterer (Figures 5(c) and 6(c)), instead of the horizontal (Figures 5(a) and 6(a)) and the -30° dipping reflectors (Figures 5(b) and 6(b)).

Dip-dependent scattering-angle-domain illumination

To overcome the limitation of the scattering-angle-domain illumination for planar reflectors discussed in the preceding section, we further decompose the illumination into dip-angle domain, resulting in dip-dependent scattering-angle-domain illumination. From equations 9 and 10, it is easy to obtain the tangent of the dip angle using either

$$\tan\alpha = -\frac{p_{m_x}}{p_{m_z}} = -\frac{k_{m_x}}{k_{m_z}}, \tag{14}$$

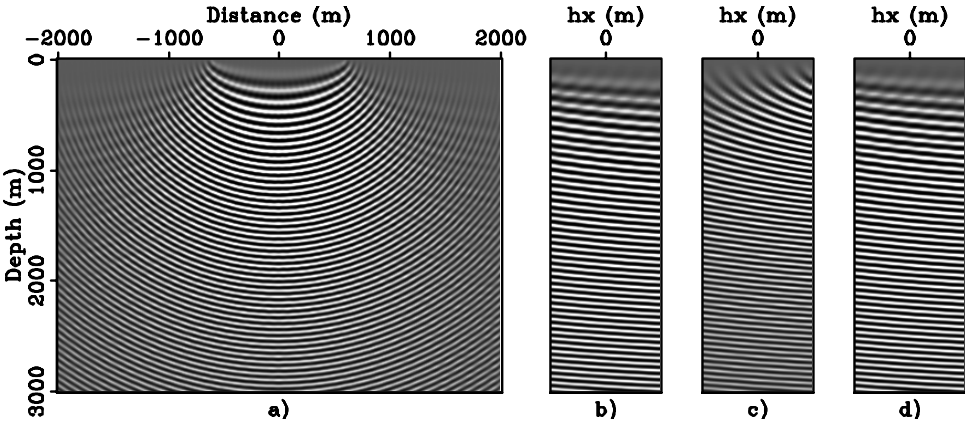

Figure 2: The real part of the subsurface-offset-domain sensitivity kernel for a constant velocity model (2000 m/s), one source at −600 m, one receiver at 600 m and one frequency (19 Hz). Panel (a) shows the kernel at zero-subsurface-offset; (b), (c) and (d) show the kernel for different spatial locations at −1000 m, 0 m and 1000 m, respectively. [**CR**]

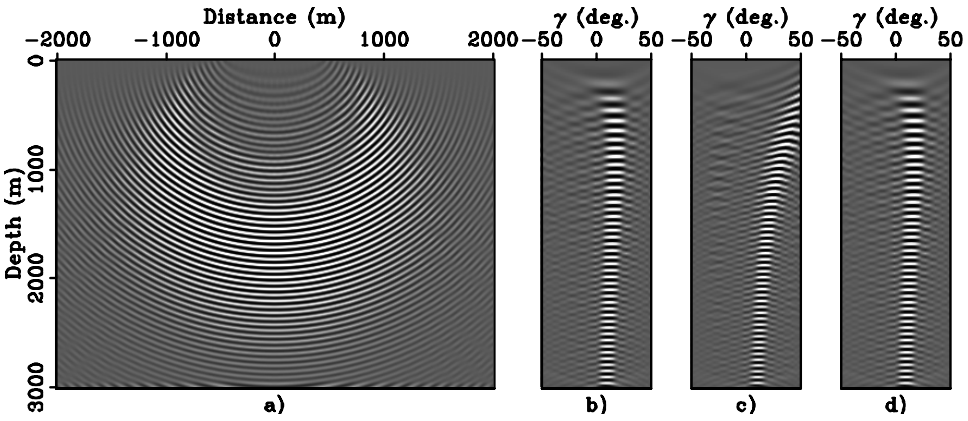

Figure 3: The real part of the scattering-angle-domain sensitivity kernel after conversion from the subsurface offset domain (Figure 2). Panel (a) shows the sensitivity kernel for a constant scattering angle 18.75°; (b), (c) and (d) show the kernel for spatial locations at −1000 m, 0 m and 1000 m, respectively. [**CR**]

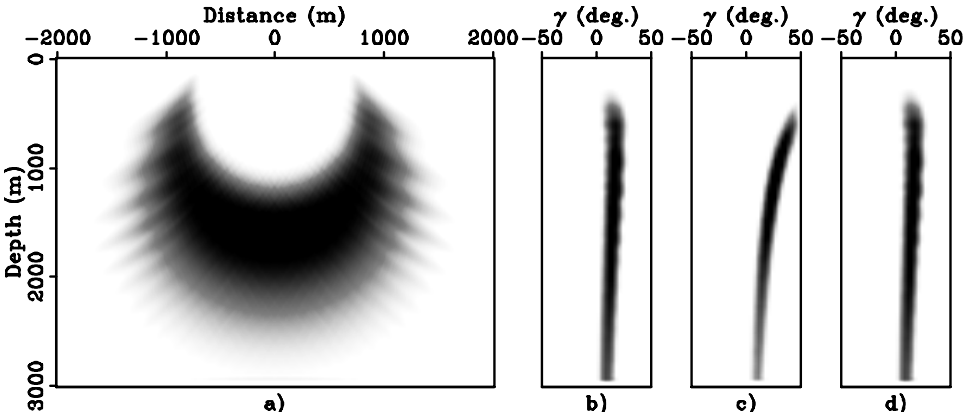

Figure 4: The single-frequency scattering-angle-domain illumination obtained using the sensitivity kernel shown in Figure 3. Panel (a) shows the illumination for scattering angle 18.75°; (b), (c) and (d) show the illumination angle gathers for spatial locations at −1000 m, 0 m and 1000 m, respectively. [**CR**]

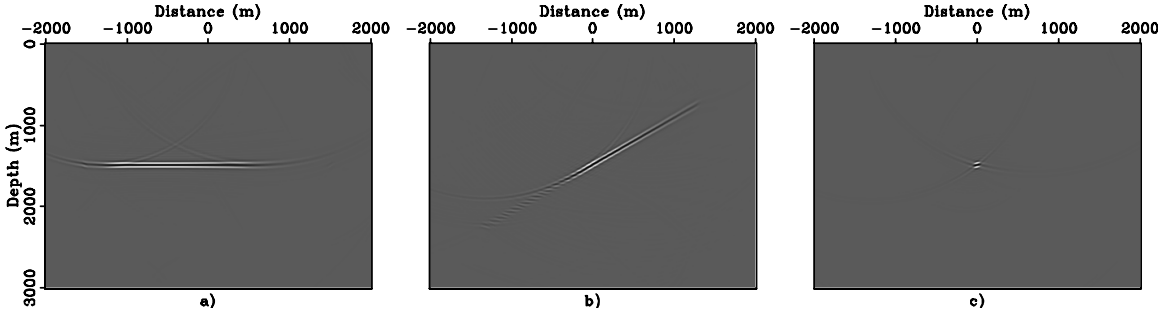

Figure 5: Migrated zero-subsurface-offset images (stacked images) for (a) a horizontal reflector, (b) a dipping reflector (−30°) and (c) a point scatterer. All images are obtained by migrating only one shot located at −600 m, where 401 receivers spread from −2000 m to 2000 m with a 10 m spacing. [**CR**]

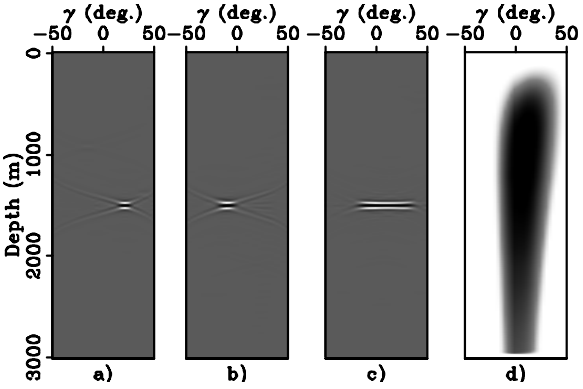

Figure 6: The scattering-angle-domain image gathers extracted at spatial location 0 m for (a) the horizontal reflector, (b) the dipping reflector and (c) the point scatterer. Panel (d) shows the scattering-angle-domain illumination gather extracted at the same spatial location. [**CR**]

or

$$\tan\alpha = \frac{p_{h_z}}{p_{h_x}} = \frac{k_{h_z}}{k_{h_x}}, \tag{15}$$

where k_{m_x}, k_{m_z} and k_{h_x}, k_{h_z} are the horizontal and vertical components of the midpoint wavenumber vector and the subsurface-offset wavenumber vector, respectively.

Dip decomposition using either equation 14 or 15 has its own pros and cons. Equation 15 is suitable for computing dip-angle gathers for sparsely isolated image points, because it does not require any CMP information, i.e., k_{mx} and k_{mz}, and outputting gathers for sparsely isolated image points may mitigate the extra computer time and storage spent in computing both the horizontal and vertical subsurface offsets, h_x and h_z. On the other hand, equation 14 is computationally less demanding, because it does not require computing vertical subsurface offsets. However, it estimates dips using the CMP information, hence a block of densely sampled image points in the CMP domain should be output to avoid dip aliasing. In the following numerical examples, we use equation 14 for dip decomposition due to the fact that it is relatively inconvenient to output vertical subsurface offsets by using one-way wave-equation-based extrapolators.

After transforming the subsurface-offset-domain sensitivity kernel into the dip-dependent scattering-angle domain, we can proceed to compute the corresponding Hessian using

$$\begin{aligned} H_{\gamma,\alpha}(\mathbf{x},\mathbf{x}',\gamma,\gamma',\alpha,\alpha') = & \sum_{\omega}\sum_{\mathbf{x}_s}\sum_{\mathbf{x}_r} W^2(\mathbf{x}_r,\mathbf{x}_s) L_{\gamma,\alpha}(\mathbf{x},\gamma,\alpha,\mathbf{x}_r,\mathbf{x}_s,\omega) \\ & \times \quad L^*_{\gamma,\alpha}(\mathbf{x}',\gamma',\alpha'\mathbf{x}_r,\mathbf{x}_s,\omega), \end{aligned} \tag{16}$$

or the illumination using

$$H_{\gamma,\alpha}(\mathbf{x},\gamma,\alpha) = \sum_{\omega}\sum_{\mathbf{x}_s}\sum_{\mathbf{x}_r} W^2(\mathbf{x}_r,\mathbf{x}_s)|L_{\gamma,\alpha}(\mathbf{x},\gamma,\alpha,\mathbf{x}_r,\mathbf{x}_s,\omega)|^2, \tag{17}$$

where $L_{\gamma,\alpha}$ is the dip-dependent scattering-angle-domain sensitivity kernel. The complete procedure can be summarized as follows:

- for fixed $\mathbf{x}_s$, $\mathbf{x}_r$ and ω, apply 3-D Fourier transform along axes x, z and h_x (if only horizontal subsurface offsets are computed)

  $$L_h(x,z,h_x,\mathbf{x}_r,\mathbf{x}_s,\omega) \rightarrow L_h(k_x,k_z,k_{h_x},\mathbf{x}_r,\mathbf{x}_s,\omega),$$

  or along z, h_x and h_z (if both horizontal and vertical subsurface offsets are computed)

  $$L_h(x,z,h_x,h_z,\mathbf{x}_r,\mathbf{x}_s,\omega) \rightarrow L_h(x,k_z,k_{h_x},k_{h_z},\mathbf{x}_r,\mathbf{x}_s,\omega);$$

- perform the mapping

$$L_h(k_x, k_z, k_{h_x}, \mathbf{x}_r, \mathbf{x}_s, \omega) \rightarrow L_{\gamma,\alpha}(k_x, k_z, \gamma, \alpha, \mathbf{x}_r, \mathbf{x}_s, \omega)$$

  according to relations 11 and 14, or

$$L_h(x, k_z, k_{h_x}, k_{h_z}, \mathbf{x}_r, \mathbf{x}_s, \omega) \rightarrow L_{\gamma,\alpha}(x, k_z, \gamma, \alpha, \mathbf{x}_r, \mathbf{x}_s, \omega)$$

  according to relations 11 and 15;

- apply inverse 2-D Fourier transform along axes k_x and k_z

$$L_{\gamma,\alpha}(k_x, k_z, \gamma, \alpha, \mathbf{x}_r, \mathbf{x}_s, \omega) \rightarrow L_{\gamma,\alpha}(x, z, \gamma, \alpha, \mathbf{x}_r, \mathbf{x}_s, \omega),$$

  or inverse 1-D Fourier transform along axis k_z

$$L_{\gamma,\alpha}(x, k_z, \gamma, \alpha, \mathbf{x}_r, \mathbf{x}_s, \omega) \rightarrow L_{\gamma,\alpha}(x, z, \gamma, \alpha, \mathbf{x}_r, \mathbf{x}_s, \omega)$$

  to obtain the dip-dependent scattering-angle-domain sensitivity kernel.

- compute either the dip-dependent scattering-angle-domain Hessian using equation 16 or the illumination using equation 17.

For the same constant velocity example, Figures 7 and 8 show the dip-dependent scattering-angle-domain illumination for 0° and -30° dip angles, respectively. The acquisition geometry is the same as that in Figure 5, i.e., 1 shot and 401 receivers. The illumination gathers (Figures 7(b) and 8(b)) successfully predict the angle-dependent illumination for both the horizontal and dipping reflectors (Figure 7(c) and Figure 8(c)).

REDUCING THE COST BY PHASE ENCODING

As mentioned in previous sections, equations 13 or 17 is intuitive to implement, however, it requires performing offset to angle transform for each component of the sensitivity kernel. This can be potentially expensive, since the cost is now proportional to the number of sources, receivers and frequencies. In this section, we show that the computational cost can be significantly reduced by using the phase-encoding technique, which was first introduced into wave-equation shot-record migration (Romero et al., 2000), and then adapted to Hessian computation by Tang (2009).

The basic idea behind phase encoding is simple, i.e., instead of computing the Green's functions sequentially with point sources as source functions, we now compute them simultaneously with encoded areal source as the source function. Thanks to the linearity of the wave equation with respect to the sources, the resultant wavefield computed using the encoded areal source can be expressed as the sum of the wavefields computed using the point sources. Therefore, instead of performing many wavefield propagations with the number of propagations being proportional to the number of

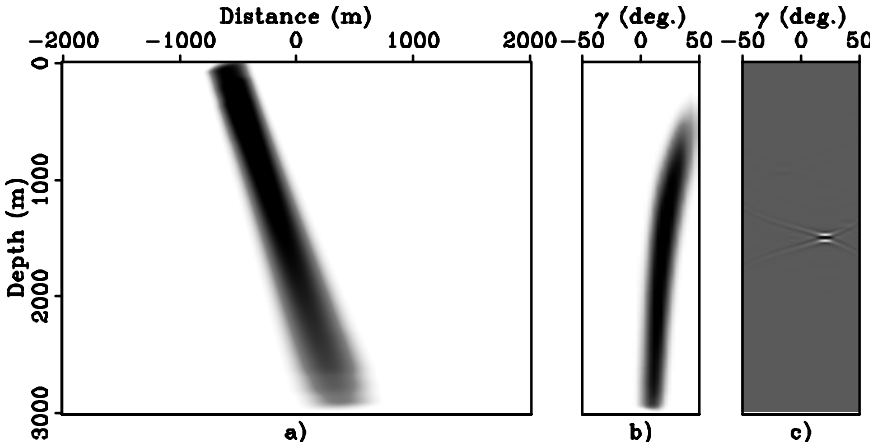

Figure 7: Dip-dependent scattering-angle-domain illumination. Panel (a) is the illumination for a constant dip angle $\alpha = 0°$ and a constant scattering angle $\gamma = 18.75°$; (b) is the illumination angle gather for a constant dip angle $\alpha = 0°$ and at spatial location $x = 0$ m; (c) is the reflectivity angle gather for the horizontal reflector extracted a $x = 0$ m, it is the same as Figure 6(a). [**CR**]

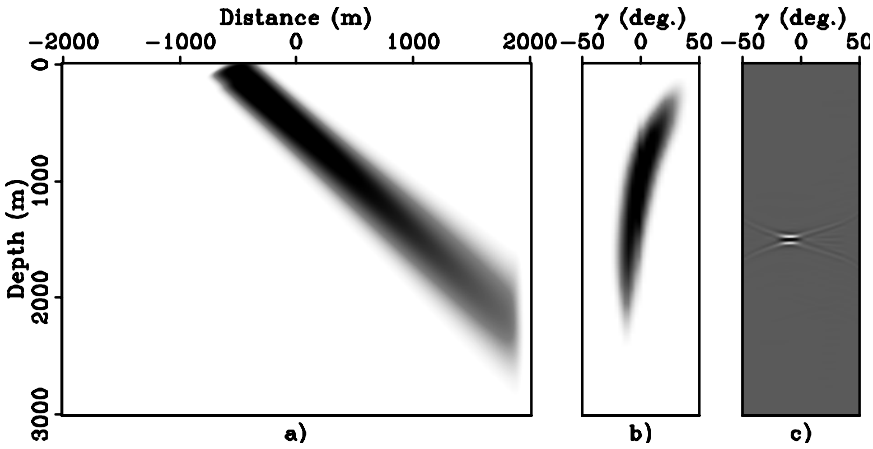

Figure 8: Dip-dependent scattering-angle-domain illumination. Panel (a) is the illumination for a constant dip angle $\alpha = -30°$ and a constant scattering angle $\gamma = 18.75°$; (b) is the illumination angle gather for a constant dip angle $\alpha = -30°$ and at spatial location $x = 0$ m; (c) is the reflectivity angle gather for the dipping reflector extracted at $x = 0$ m, it is the same as Figure 6(b). [**CR**]

point sources, by using the encoded areal sources, we reduce the number of wavefield propagations to just one, drastically reducing the computational cost. The encoding can be done in the receiver domain, which is suitable for any acquisition geometry, or in both receiver and source domain, which is suitable for land or ocean-bottom-node acquisition geometry (Tang, 2009). One drawback of the phase-encoding method, however, it that it generates crosstalk artifacts (Tang, 2009). The crosstalk can be attenuated by carefully choosing the encoding functions, such as plane-wave phase-encoding function, random phase-encoding function or a mix of the two (Tang, 2008a).

Figure 9 shows the exact scattering-angle-domain illumination for the same constant velocity model and the 1-shot-401-receiver configuration (Figure 6). It is obtained using the point source Green's function and is very expensive, and we show it here for bench-marking purposes. Figure 10 shows the result obtained by assembling the receiver-side Green's functions but without any phase-encoding function applied. The result is apparently dominated by crosstalk artifacts and has a completely wrong illumination pattern. The crosstalk artifacts can be effectively attenuated using the random phase-encoding function, as shown in Figures 11, 12 and 13, which are computed using different number of random realizations. Although not shown here, similar results can be obtained for the dip-dependent scattering-angle-domain illumination.

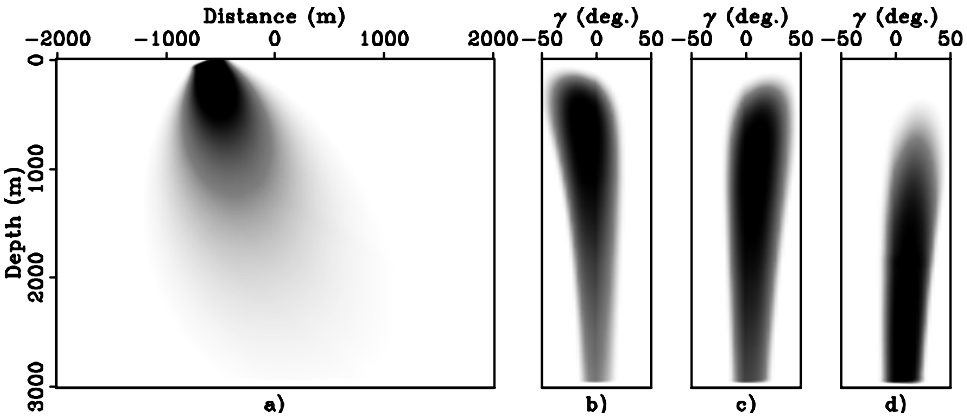

Figure 9: Exact scattering-angle-domain illumination. (a) shows the illumination for scattering angle 18.75°; (b), (c) and (d) shows the illumination angle gathers for spatial locations −1000 m, 0 m and 1000 m, respectively. [**CR**]

NUMERICAL EXAMPLES

We test our methods on the Sigsbee2A model, where the complex salt body and limited acquisition geometry result in uneven subsurface illumination below the salt. The velocity field shown in Figure 14 is used for computing various angle-domain reflectivity images and illumination. Figure 15 shows the scattering-angle-domain reflectivity image. Note the holes in the scattering-angle gathers (Figures 15(b)-(g))

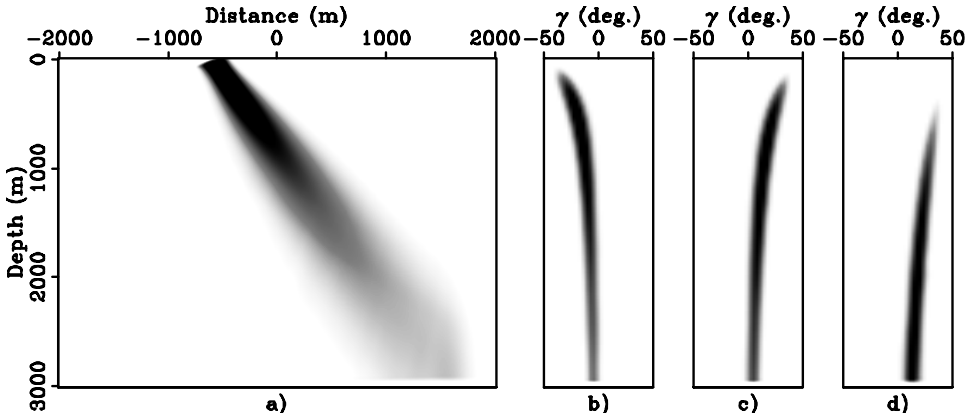

Figure 10: Scattering-angle-domain illumination with crosstalk artifacts. View descriptions are the same as Figure 9. [**CR**]

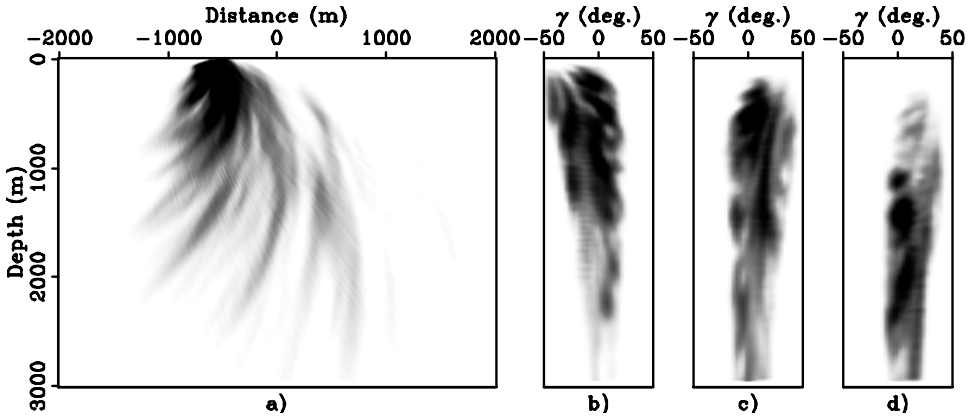

Figure 11: Receiver-side encoded scattering-angle-domain illumination with 1 random realization. View descriptions are the same as Figure 9. [**CR**]

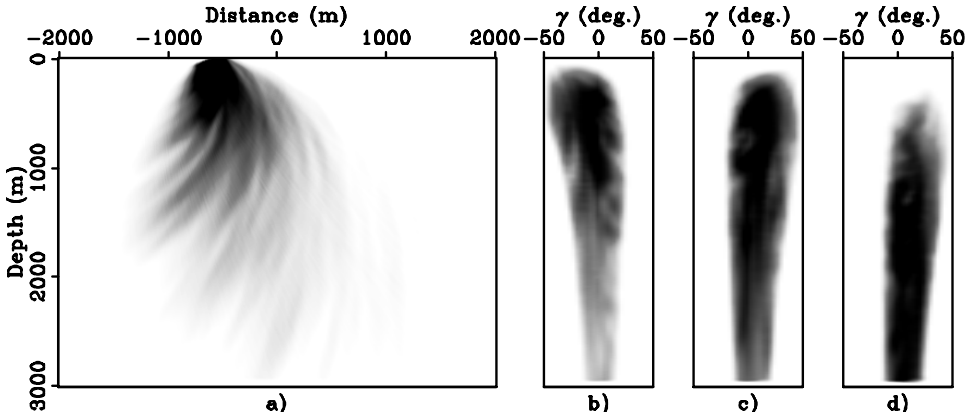

Figure 12: Receiver-side encoded scattering-angle-domain illumination with 5 random realizations. View descriptions are the same as Figure 9. [**CR**]

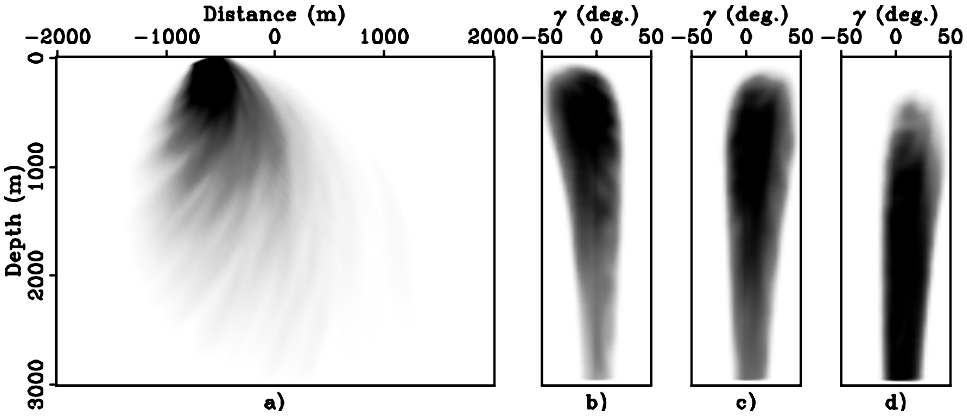

Figure 13: Receiver-side encoded scattering-angle-domain illumination with 20 random realizations. View descriptions are the same as Figure 9. [**CR**]

caused by uneven illumination. This phenomenon should conform with the angle-domain illumination. As expected, the scattering-angle-domain illumination (Figure 16) fails to accurately predict the illumination pattern for planar reflectors, e.g., the horizontal reflector at depth 29500 ft, although it is very accurate for the point scatterers locatd at depth 25000 ft. We further decompose the image and illumination into dip-dependent scattering-angle domain. The illumination pattern (Figure 18) now conforms very well with the image of the planar reflectors (Figure 17) as well as the reflectors that have a zero dip in Figure 15.

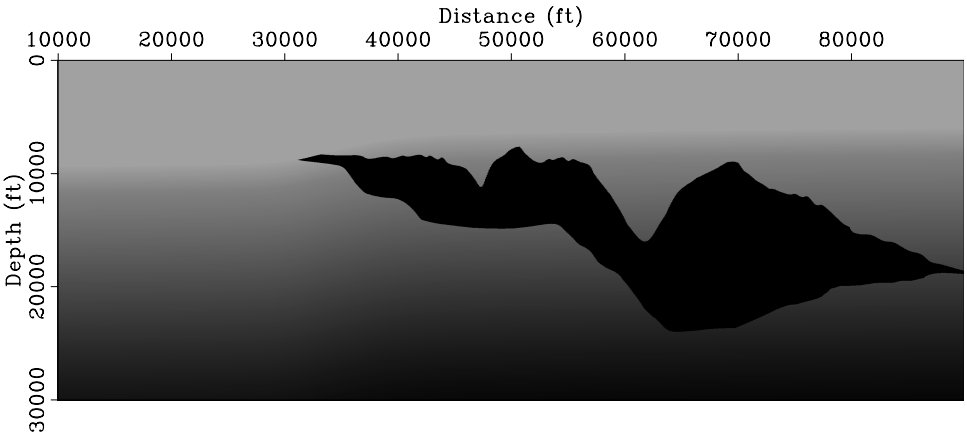

Figure 14: Sigsbee2A velocity model used for migration and illumination computation. [**ER**]

CONCLUSIONS

We present a method for computing the angle-domain illumination, or more generally, the angle-domain Hessian. The method takes advantage of the relation among

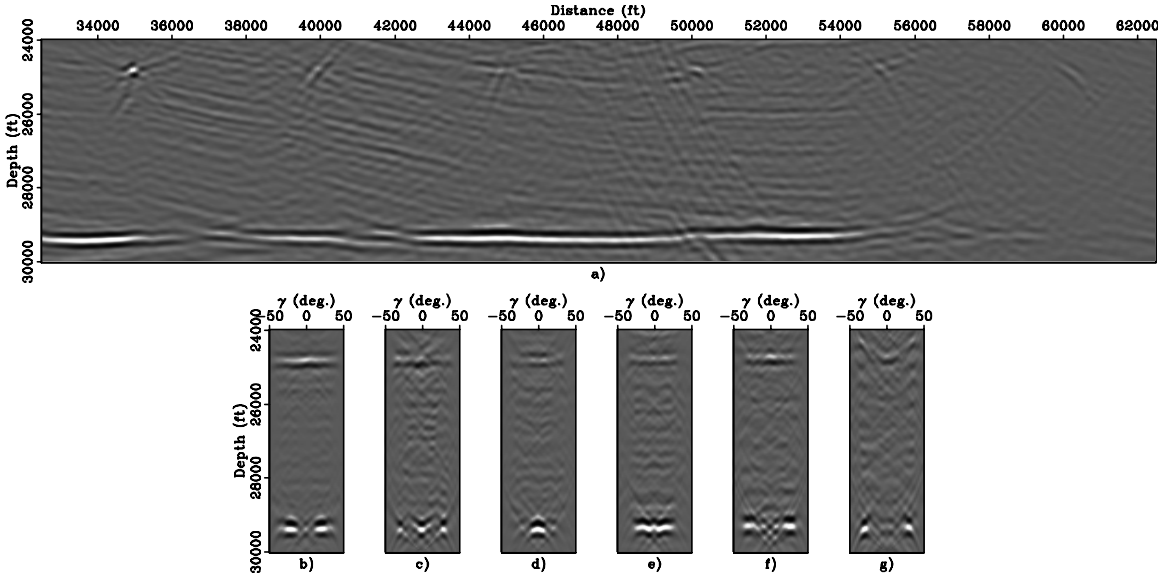

Figure 15: Scattering-angle-domain reflectivity image for the Sigsbee2A model. Panel (a) shows the image with scattering angle $\gamma = 0°$; (b), (c), (d), (e), (f) and (g) show the scattering angle gathers extracted at spatial locations 35000 ft, 40000 ft, 45000 ft, 50000 ft, 55000 ft and 60000 ft, respectively. [**CR**]

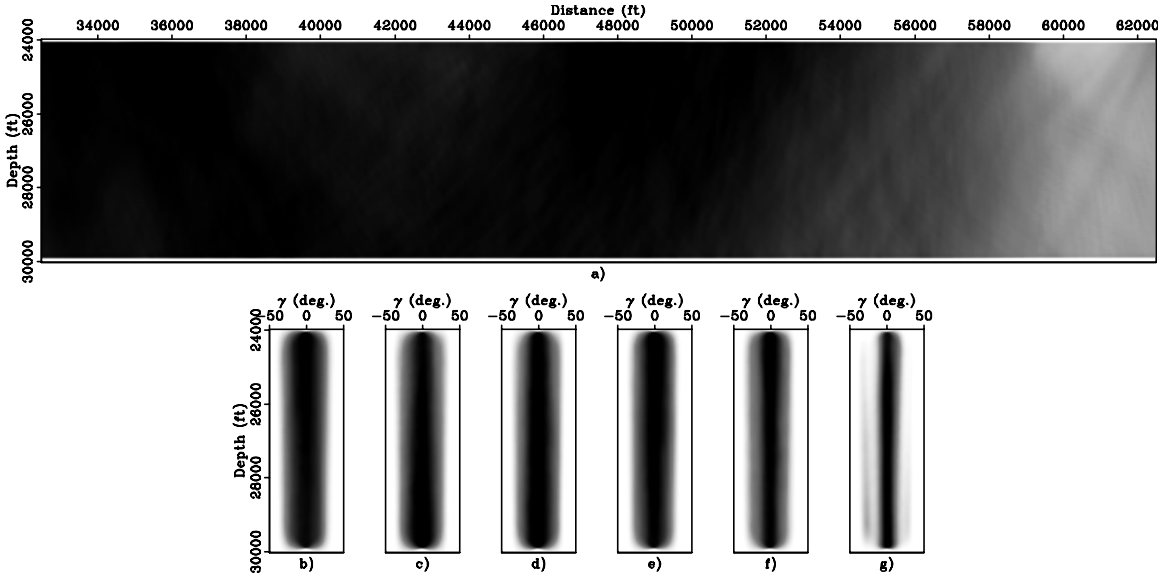

Figure 16: Scattering-angle-domain illumination for the Sigsbee2A model. View descriptions are the same as Figure 15. [**CR**]

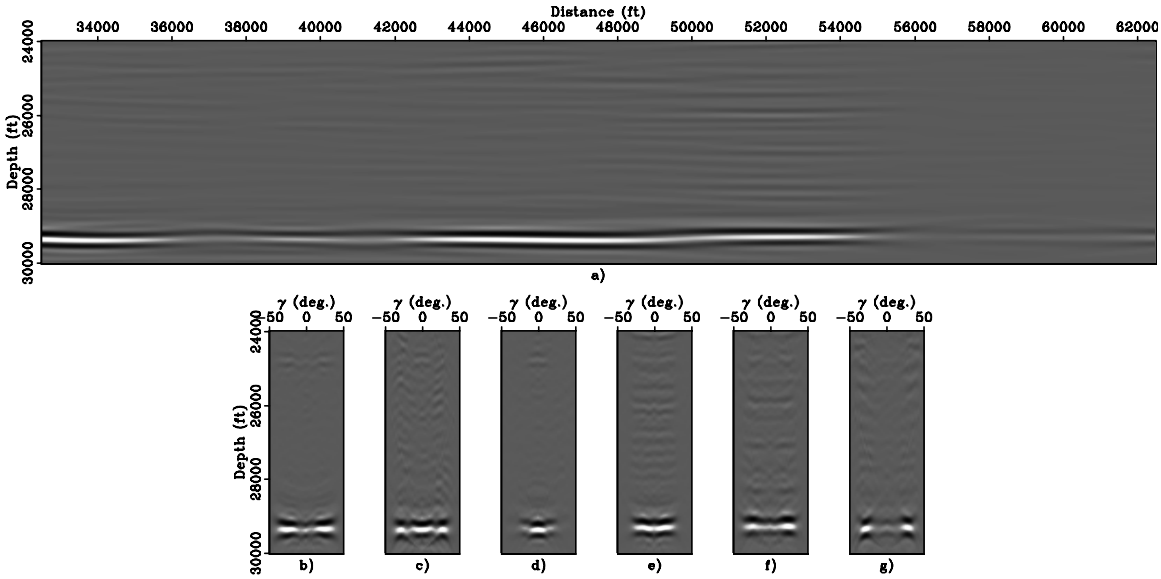

Figure 17: Dip-dependent scattering-angle-domain reflectivity image for the Sigsbee2A model. Panel (a) shows the image with scattering angle $\gamma = 0°$ and dip angle $\alpha = 0°$; (b), (c), (d), (e), (f) and (g) show the scattering angle gathers extracted at spatial locations 35000 ft, 40000 ft, 45000 ft, 50000 ft, 55000 ft and 60000 ft, respectively. [**CR**]

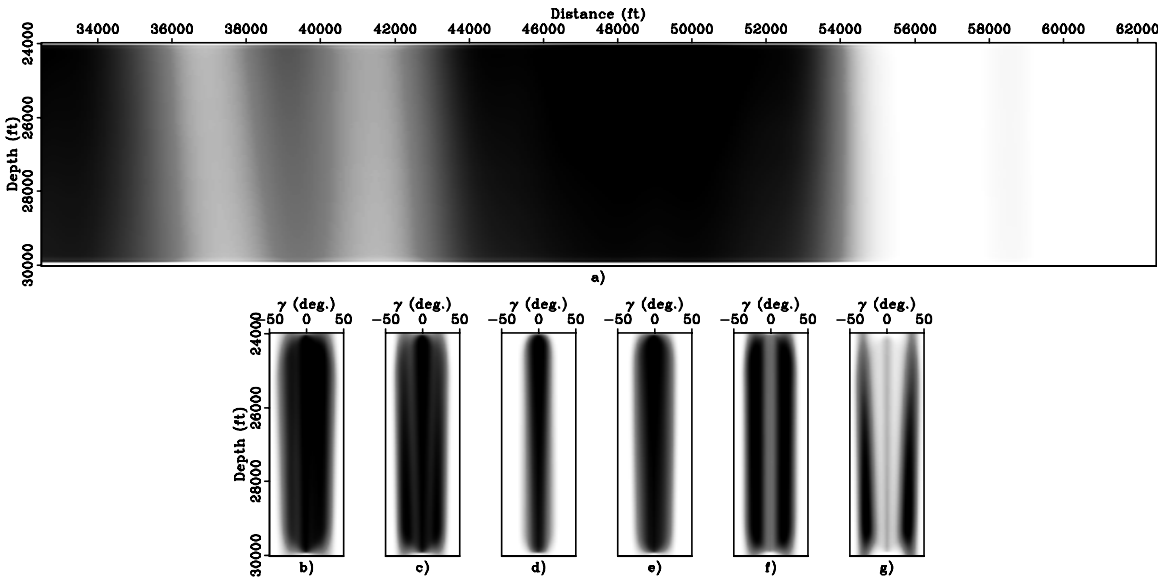

Figure 18: Scattering-angle-domain illumination for the Sigsbee2A model. View descriptions are the same as Figure 17. [**CR**]

scattering angles, dip angles, CMP wavenumbers and subsurface-offset wavenumbers, and uses a simple Fourier-domain mapping to transform from subsurface offset domain into angle domain. Our method can decompose the illumination or Hessian into either scattering-angle domain suitable for point scatterers, or dip-dependent scattering-angle domain suitable for planar reflectors. A straight forward implementation of our method, however, can be very expensive. We show how the cost can be drastically reduced by using the phase-encoding technique. Numerical examples demonstrate that our method can produce accurate illumination estimation for both point scatterers and planar reflectors, and therefore, it is useful for application related to AVA analysis or robust migration velocity residual parameter estimation.

REFERENCES

Bear, G., C.-P. Lu, R. Lu, D. Willen, and I. Watson, 2000, The construction of subsurface illumination and amplitude maps via ray tracing: The Leading Edge, **19**, 726–728.

Clapp, M. L., 2005, Imaging Under Salt: Illumination Compensation by Regularized Inversion: PhD thesis, Stanford University.

Nemeth, T., C. Wu, and G. Schuster, 1999, Least-squares migration of incomplete reflection data: Geophysics, **64**, 208–221.

Rickett, J. E. and P. C. Sava, 2002, Offset and angle-domain common image-point gathers for shot-profile migration: Geophysics, **67**, 883–889.

Romero, L. A., D. C. Ghiglia, C. C. Ober, and S. A. Morton, 2000, Phase encoding of shot records in prestack migration: Geophysics, **65**, 426–436.

Sava, P. C. and S. Fomel, 2003, Angle-domain common-image gathers by wavefield continuation methods: Geophysics, **68**, 1065–1074.

Schneider, W. A. and J. G. A. Winbow, 1999, Efficient and accurate modelling of 3-d seismic illumination: SEG Technical Program Expanded Abstracts, **18**, 633–636.

Tang, Y., 2008a, Modeling, migration and inversion in the generalized source and receiver domain: **SEP-136**, 97–112.

———, 2008b, Wave-equation Hessian by phase encoding: **SEP-134**, 1–24.

———, 2009, Target-oriented wave-equation least-squares migration/inversion with phase-encoded Hessian: Geophysics, **74**, WCA95–WCA107.

Valenciano, A., 2008, Imaging by Wave-equation Inversion: PhD thesis, Stanford University.

Xie, X.-B., S. Jin, and R.-S. Wu, 2006, Wave-equation-based seismic illumination analysis: Geophysics, **71**, S169–S177.